PERGAMON

International Journal of Heat and Mass Transfer 46 (2003) 889–902

International Journal of
HEAT and MASS
TRANSFER

www.elsevier.com/locate/ijhmt

Friction and heat transfer characteristics of flow through square duct with twisted tape insert

S. Ray [a,*], A.W. Date [b]

[a] Department of Mechanical Engineering, Jadavpur University, Kolkata 700 032, India
[b] Department of Mechanical Engineering, Indian Institute of Technology, Bombay Powai, Mumbai 400 076, India

Received 15 June 1999; received in revised form 10 May 2002

Abstract

This paper presents numerical prediction of characteristics of laminar, as well as, turbulent flow and heat transfer in a square sectioned duct inserted with a twisted tape, whose width equals the length of the duct side. The heat transfer characteristics are predicted under axially and peripherally constant wall heat flux conditions. As such, the flow and heat transfer are periodically fully developed in axial direction. Correlations for friction factor and Nusselt number are derived from the predicted data. The correlation for friction is compared with the experimental data, which are found to be in reasonably good agreement with each other, for both laminar and turbulent flows.

1. Introduction

Insertion of twisted tapes in circular tubes provides a simple passive technique for enhancing the convective heat transfer coefficient on the tube side of a heat exchanger. Twisted tape inserts are used to achieve compact heat exchangers, as well as, to prevent hot spots in high heat flux transfer situations encountered with gas flows.

A duct of square cross-section provides higher surface to volume ratio than a circular tube. Further, if a square duct is inserted with a twisted tape, whose width equals the side of the duct, the flow becomes periodically fully developed with the distance of periodicity equals to 90° rotation of the tape. Similarly, the heat transfer also attains periodically fully developed state. Thus, both the flow and heat transfer are under continuous state of *periodic development*. Therefore, compared to a circular tube with a twisted tape insert, a higher thermal-hydraulic performance can be expected from a square duct with a twisted tape insert.

Fig. 1a shows the layout of a square duct with a full-length twisted tape. The pitch for 180° rotation is H. The width of the tape equals length of the side, a, of the duct. The tape thickness is δ, with $\delta/a \approx 1/30$. The twisted tape thus makes contact with the duct sides at every $H/2$ distance (or, after every 90° rotation); in between, the tape looses contact with duct sides providing free flow area on either side of its width (Fig. 1b).

It will be appreciated that at any cross-section both flow and heat transfer will exhibit *cross-mirror-image* symmetry. As such, attention may be focussed on a cross-section on any one side of the tape. Such a cross-section, although having constant area (i.e., half of the cross-sectional area of square duct) will have different shapes at different axial locations. The same shape and orientation will however repeat after every 2H distance in the axial direction.

Mano et al. [1] and Bhadsavle [2] have presented experimentally determined correlations of friction factors for flow in a square duct with twisted tape insert. On comparison, however, it is observed that the correlations are at considerable variance with each other [3]. These correlations and the correlation obtained from the present study are compared with the experimental data in Section 4.4, which clearly show this disagreement. The purpose of this paper is therefore to present experimentally and numerically determined data covering a wide range of Reynolds number, Prandtl number and twist ratio ($Y = H/a$).

---

[*] Corresponding author. Tel./fax: +91-33-414-6890.
E-mail address: juhp_sray@yahoo.co.in (S. Ray).

0017-9310/03/$ - see front matter © 2002 Elsevier Science Ltd. All rights reserved.
PII: S0017-9310(02)00355-1

Nomenclature

a	side of the square duct, m
A_c	cross-sectional area of the duct, m^2
B_j	body force in the jth momentum equation
C_i	constants ($i = \mu, 1, 2$)
C_p	specific heat, J/kg K
dA_i	elemental area, perpendicular to $\xi_i =$ constant surface, m^2
D	diffusion coefficient in the ϕ conservation equation
D_i	general diffusion coefficient
e	turbulent kinetic energy
E	constant in law of wall
f	friction factor
G	production of turbulent kinetic energy
D_i	contravariant mass velocity, ρU_i ($i = 1, 2, 3$), kg/m^2 s
h_{x_3}, $\bar{h}$	local and average heat transfer coefficients, W/m^2 K
H	pitch for 180° rotation, m
J	Jacobian of the coordinate transformation
k	thermal conductivity, W/m K
n	normal direction
Nu_{x_3}, Nu	local and average Nusselt number
p	pressure, N/m^2
$\bar{p}$	control volume averaged pressure
p'	total pressure correction
p'_m	mass conserving pressure correction
p'_s	smoothing pressure correction
Pr	Prandtl number
q_w	wall heat flux, W/m^2
q_k^{ϕ}	scalar fluxes of ϕ
Re	Reynolds number
S_c	duct perimeter, m
S_w	swirl parameter
S_{ϕ}	source term in the ϕ conservation equation
t	time, s
T	temperature, K
T_b	bulk temperature, K
T_w, $\overline{T}_w$	local and average wall temperature, K
u_i	Cartesian velocity components ($i = 1, 2, 3$), m/s
u_{τ}	friction velocity
U_i	contravariant velocity components ($i = 1, 2, 3$), m^3/s
$V_{x_i}^{t}$	ith component of tangential velocity vector, m/s
x_i	Cartesian coordinates
y^+	wall coordinate
Y	twist ratio (H/a)
Greek symbols	
β_p	mean axial pressure gradient, N/m^3
β_j^i	geometric factors
δ	tape thickness, m
Δn	normal distance between nodes
ε	dissipation
ϕ	general variable
κ	constant in law of wall
ρ	density, kg/m^3
ξ_i	curvilinear coordinates ($i = 1, 2, 3$)
μ	dynamic viscosity, N s/m^2
μ_{eff}	effective viscosity, N s/m^2
μ_t	turbulent viscosity, N s/m^2
θ	twist angle, rad
τ_{ij}	shear stress, N/m^2
σ	turbulent Prandtl number

Section 2 of this paper provides the mathematical formulation of the problem. Section 3 discusses the computational aspects. The results are discussed in Section 4 and the conclusions are reported in Section 5.

2. Mathematical formulation

2.1. Governing equations

Consider conservation equations in Cartesian coordinates (x_1, x_2, x_3), in which, x_3 is aligned with the axis of the duct and x_1 and x_2 are as shown in Fig. 1b. When these equations are transformed to curvilinear coordinates (ξ_1, ξ_2, ξ_3), they can be written in the following general form:

$$J\frac{\partial}{\partial t}(\rho\phi) + \sum_{i=1}^{3}\frac{\partial}{\partial \xi_i}\left[\rho U_i \phi - D_i \frac{\partial \phi}{\partial \xi_i}\right] = S_{\phi} \qquad (1)$$

where D_i and S_{ϕ} are interpreted in Table 1. Further definitions are given in Table 2. The tables show that when $\phi = 1$, mass conservation equation is retrieved. The momentum equations are written for Cartesian velocity components ($\phi = u_j$). It is important to note that the term $D_i\,\partial\phi/\partial\xi_i$ represents the dummy diffusion normal to $\xi_i =$ constant surfaces. The true Cartesian diffusion is included in the source terms through gradient of stresses, τ_{ij}, and scalar fluxes, q_k^{ϕ}. For turbulent flows, the high turbulent Reynolds number k–ε model of turbulence is employed with model constants, $C_{\mu} = 0.09$, $C_1 = 1.44$, $C_2 = 1.92$, $\sigma_e = 1.0$, $\sigma_{\varepsilon} = 1.3$ and $\sigma_T = 0.9$ [4,5].

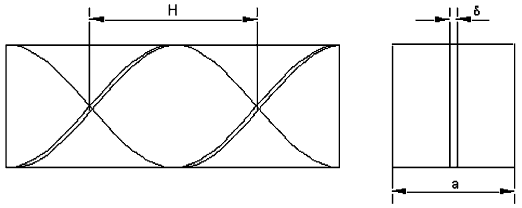

(a) **Schematic view of the square duct with twisted tape insert.**

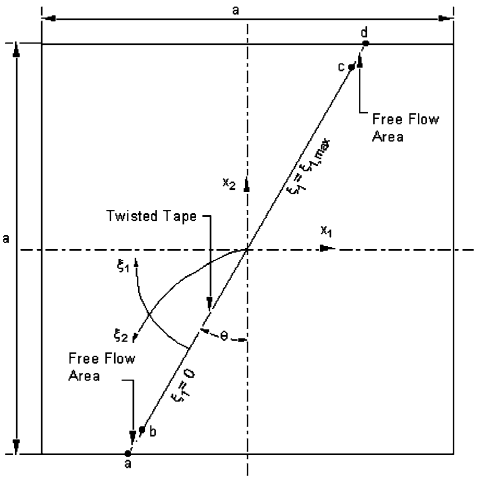

(b) **Cross section of the square duct at a twist angle θ.**

Fig. 1. Geometry of the square duct with twisted tape insert.

In Eq. (1), ξ_3 coincides with x_3, but ξ_1 and ξ_2 are generated by using the method of elliptic grid generation suggested Sorenson [6] at every cross-section in the periodic domain. Fig. 2 shows typical grids used for laminar and turbulent flows, at a cross-section, where $\theta = 22.5°$.

2.2. Boundary conditions

In the present method, the solutions are obtained only for the interior points. This is done by eliminating the boundary points from the discretised equations for near boundary control volume, using the boundary conditions. The boundary values are evaluated subsequently from the solutions of the interior points. The boundary conditions for the present problem can be classified into two categories:

1. wall condition,
2. periodicity condition.

2.2.1. Wall boundary conditions

On the duct and the tape surfaces, all the velocities are set equal to zero to implement the no-slip condition. The duct is also subjected to a constant axial peripheral and axial wall heat flux. Therefore, the boundary conditions can be expressed as

Table 1
Meaning of D_i and S_ϕ

ϕ	D_i	S_ϕ
1	0	0
U_j	$\mu_{\text{eff}}\,\mathrm{d}A_i^2/J$	$-\sum_{k=1}^{3}\beta_k^j\,\partial p/\partial\xi_k + \sum_{i=1}^{3}\partial\left[\sum_{k=1}^{3}\beta_i^k\tau_{jk} - D_i\,\partial u_j/\partial\xi_i\right]\Big/\partial\xi_i + B_j$
T	$\Gamma_{\text{eff},T}\,\mathrm{d}A_i^2/J$	$-\sum_{i=1}^{3}\partial\left[\sum_{k=1}^{3}\beta_i^k q_k^T + D_i\,\partial T/\partial\xi_i\right]\Big/\partial\xi_i$
e	$\Gamma_{\text{eff},k}\,\mathrm{d}A_i^2/J$	$G - \rho\varepsilon - \sum_{i=1}^{3}\partial\left[\sum_{k=1}^{3}\beta_i^k q_k^e + D_i\,\partial e/\partial\xi_i\right]\Big/\partial\xi_i$
ε	$\Gamma_{\text{eff},\varepsilon}\,\mathrm{d}A_i^2/J$	$(\varepsilon/e)(C_1 G - C_2\rho\varepsilon) - \sum_{i=1}^{3}\partial\left[\sum_{k=1}^{3}\beta_i^k q_k^\varepsilon + D_i\,\partial\varepsilon/\partial\xi_i\right]\Big/\partial\xi_i$

Table 2
Terms in Table 1

Symbol	Meaning	Definition
U_i	Contravariant flow velocity	$\sum_{j=1}^{3}\beta_i^j u_j$
τ_{ij}	Stresses	$(\mu_{\text{eff}}/J)\sum_{k=1}^{3}(\beta_k^i\,\partial u_j/\partial\xi_k + \beta_k^j\,\partial u_i/\partial\xi_k) - \frac{2}{3}\rho\delta_{ij}e$
q_k^ϕ	Flux of ϕ	$-(\Gamma_{\text{eff},\phi}/J)\sum_{j=1}^{3}\beta_j^k\,\partial\phi/\partial\xi_j$
μ_{eff}	Effective viscosity	$\mu + \mu_{\text{t}} = \mu + c_\mu\rho e^2/\varepsilon$
$\Gamma_{\text{eff},\phi}$	Effective diffusivity for scalar ϕ	$(\mu/Pr) + c_\mu\rho e^2/\varepsilon\sigma_\phi$
β_j^i	Geometric coefficients	$(\partial x_j/\partial\xi_k)(\partial x_k/\partial\xi_i) - (\partial x_j/\partial\xi_i)(\partial x_k/\partial\xi_k)$, $k \neq i, j$
J	Cell volume	$\sum_{k=1}^{3}\beta_i^k\,\partial x_k/\partial\xi_i$, $i = 1, 2$ or 3
$\mathrm{d}A_i$	Cell-face area	$[\sum_{j=1}^{3}(\beta_i^j)^2]^{1/2}$
G	Production of T.K.E.	$\tau_{ij}\sum_{k=1}^{3}(\beta_k^j/J)(\partial u_i/\partial\xi_k)$
B_j	Body force	

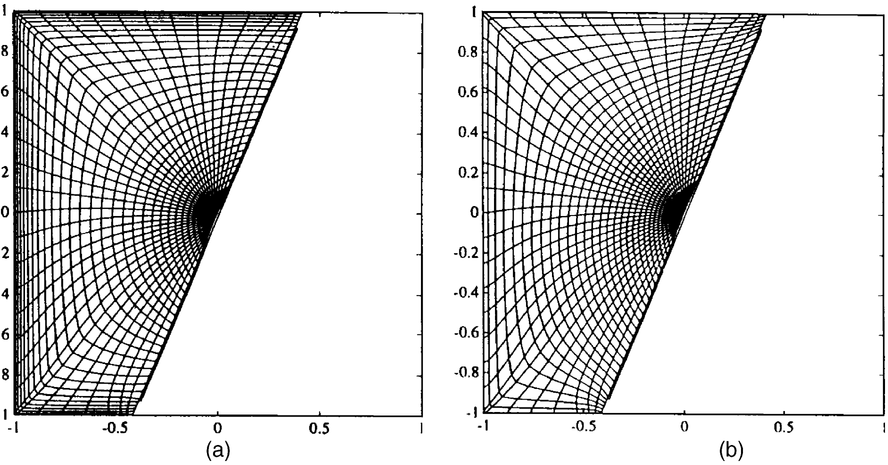

(a) (b)

Fig. 2. Typical numerical grid for $\theta = 45°$: (a) laminar flow and (b) turbulent flow.

$$u_j = 0, \quad \text{for } j = 1,2,3 \tag{2}$$

and

$$-k\,\partial T/\partial n = q_w \quad \text{at } \xi_2 = \xi_{2,\max} \tag{3}$$

where "n" denotes the normal derivative and q_w represents the applied wall heat flux. Therefore, $q_w = 0$, on the tape surface (at $\xi_1 = 0, \xi_{1,\max}$) as the tape is considered to be insulated.

For turbulent flows, wall function approach is adopted. On a solid boundary of constant ξ_i, in order to calculate the stresses (and hence, the source terms), the tangential velocity component ($V^t_{x_l}$, the x_l component of the tangential velocity vector), normal distance ($|\Delta n|$) and the effective viscosity (μ_{eff}) are required. The first two quantities remain same for both laminar and turbulent flows and are given by

$$V^t_{x_l} = u_l\left[1 - \left(\frac{\beta_i^l}{\mathrm{d}A_i}\right)^2\right] - \sum_{n=1,n\neq l}^{3} u_n\left(\frac{\beta_i^l}{\mathrm{d}A_i}\right)\left(\frac{\beta_i^n}{\mathrm{d}A_i}\right) \tag{4}$$

$$\Delta n = \frac{\sum_{n=1}^{3}\beta_i^n(\partial x_n/\partial\xi_i)}{\sqrt{\sum_{n=1}^{3}(\beta_i^n)^2}} \tag{5}$$

For laminar flows, μ_{eff} is simply replaced by μ. However, for turbulent flows, when $y^+(= yu_\tau/\nu) \geqslant 11.6$, this is obtained as

$$\frac{\mu_{\text{eff}}}{|\Delta n|} = \frac{\rho u_\tau \kappa}{\ln(Ey^+)} \tag{6}$$

where the friction velocity, u_τ, is obtained as

$$u_\tau = C_\mu^{1/4} e_P^{1/2} \tag{7}$$

In the energy equation, the wall heat flux is expressed as

$$q_w = k_{\text{eff}}\frac{(T_B - T_P)}{|\Delta n|} \tag{8}$$

where T_B and T_P are the temperatures of the boundary and the near boundary nodes respectively and q_w is considered to be positive, if it is added to the computational domain. For laminar flow, $k_{\text{eff}} = k$. For turbulent flow, k_{eff} is recovered from the law of the wall for temperature, given by

$$T_P^+ = \frac{T_B - T_P}{q_w/\rho C_p u_\tau} = \sigma_T(\mathrm{PF} + u_P^+) \tag{9}$$

where the function PF is considered as

$$\mathrm{PF} = 9.24\left[\left(\frac{Pr}{\sigma_T}\right)^{0.75} - 1\right] \tag{10}$$

Thus, from Eqs. (8) and (9), k_{eff} is obtained as

$$k_{\text{eff}} = \frac{\rho C_p u_\tau|\Delta n|}{\sigma_T(\mathrm{PF} + u_P^+)} \tag{11}$$

In the "wall function" approach, the source term of the turbulent kinetic energy equation, S_e for the near boundary node is calculated as

$$\begin{aligned} S_e &= J(G - \rho\varepsilon) = J\left[\tau_{\text{tot}}\left.\frac{\partial V^t}{\partial n}\right|_B - \rho\bar{\varepsilon}_P\right] \\ &= J\left[\frac{\mu_{\text{eff}}}{(\Delta n)^2}\sum_{i=1}^{3}(V^t_{x_i,B} - V^t_{x_i,P})^2 - \rho\bar{\varepsilon}_P\right] \end{aligned} \tag{12}$$

where $\bar{\varepsilon}_P$ is the average dissipation at node "P" and is obtained as

$$\bar{\varepsilon}_P = \frac{1}{\Delta n}\int_0^{\Delta n}\varepsilon\,\mathrm{d}n = \frac{u_\tau^3}{\kappa\Delta n}\ln(Ey^+) = \frac{\rho u_\tau^2}{\mu_{\text{eff}}}C_\mu^{1/2}e_P \tag{13}$$

For ε equation, the value at node "P" is frozen at $u_\tau^3/\kappa\Delta n$.

2.2.2. Axial periodicity

In order to model the axial periodicity, the pressure in Cartesian coordinates is written as

$$p(x_1,x_2,x_3) = -\beta x_3 + P(x_1,x_2,x_3) \tag{14}$$

In the above equation, $\beta_p(=\Delta\bar{p}/2H)$ is the mean axial pressure gradient over the periodic distance $2H$. With the introduction of the new pressure, P, the transformed x_3 momentum equation now contains an additional source term, $J\beta_p$. In all the momentum equations, p is replaced by P.

Computations are first carried out by applying the boundary conditions for long periodicity, over a length $2H$, to verify the existence of short periodicity over $H/2$. In the former case, the boundary conditions at $x_3 = 0$, or, $\xi_3 = 0$ and $x_3 = 2H$, or, $\xi_3 = \xi_{3,\max}$ of the computational domain are represented by

$$u_j|_{\xi_3=0} = u_j|_{\xi_3=\xi_{3,\max}} \quad \text{for } j = 1,2,3 \tag{15a}$$

$$(e,\varepsilon,P)|_{\xi_3=0} = (e,\varepsilon,P)|_{\xi_3=\xi_{3,\max}} \tag{15b}$$

$$T|_{\xi_3=0} + \Delta T_3 = T|_{\xi_3=\xi_{3,\max}} \tag{15c}$$

where ΔT_3 is the temperature rise in the axial direction, over the length of periodicity. For shorter periodicity ($x_{3,\max} = H/2$), the conditions for u_1 and u_2 only change and they are given as

$$u_1|_{\xi_3=0} = -u_2|_{\xi_3=\xi_{3,\max}} \tag{16a}$$

$$u_2|_{\xi_3=0} = u_1|_{\xi_3=\xi_{3,\max}} \tag{16b}$$

2.2.3. Cross-periodicity

The cross-periodicity condition in the fluid domain (free flow area) for the half duct, at any axial station, is represented as

$$u_{1,2}|_{\xi_1=0} = -u_{1,2}|_{\xi_1=\xi_{1,\max}} \tag{17a}$$

$$(u_3,e,\varepsilon,T,P)|_{\xi_1=0} = (u_3,e,\varepsilon,T,P)|_{\xi_1=\xi_{1,\max}} \tag{17b}$$

3. Computational aspects

3.1. Method of solution

Governing equations (1) are discretised by control volume based finite difference technique on non-staggered grid. The discretised equations are solved sequentially, in which, following the strategy adopted in the SIMPLE algorithm [7,8], the pressure distribution is recovered by solving a pressure correction equation, that implicitly satisfies the mass conservation equation.

On non-staggered grid, however, the pressure gradient evaluation at a node becomes decoupled from the velocity at the node, which, in turn, results in checker board prediction of pressure on coarse grids [9]. But since the overall algorithm is of the SIMPLE type this difficulty is removed by solving an equation for *total* pressure correction (p'), which reads as

$$\frac{\partial}{\partial \xi_i}\left(D_i \frac{\partial p'}{\partial \xi_i}\right) = \frac{\partial G_i}{\partial \xi_i} \quad \text{for } i = 1,2,3 \tag{18}$$

where G_i are the contravariant mass velocity and D_i are the appropriate coefficients. The *mass conserving* pressure correction (p'_m) is recovered from the *total* pressure correction as follows:

$$p'_\mathrm{m} = p' - p'_\mathrm{s} \tag{19}$$

where p'_s is the *smoothing* pressure correction, which is defined as

$$p'_\mathrm{s} = 0.5(p - \bar{p}) \tag{20}$$

and $\bar{p}$ is the control volume averaged pressure. Complete derivation of the above smoothing procedure can be found in [10,11].

3.2. Convergence and accuracy

The discretised equations are solved by an iterative process. Since, the fluid properties are assumed to be uniform, the equations for flow variables are solved first, followed by the solution of the energy equation. The convergence is checked by the L_2 norm of the residues; i.e., if $R^\phi_{i,j,k}$ is the residual in the discretised equation for variable ϕ at node (i,j,k), then, $L_2 = [\sum_{i,j,k}(R^\phi_{i,j,k})^2]^{1/2}$. For velocities and pressure, convergence is declared when $L_2 \leqslant 10^{-4}$; and for temperature, $L_2 \leqslant 10^{-6}$. The laminar flow solutions typically converged within 300–600 iterations; the number of iterations increasing with Reynolds number and decreasing with twist ratio. Global under-relaxation factor, $\alpha = 0.5$, proved to be adequate. Convergence of turbulent flow equations however required special care. For first 1000 iterations, computations are carried out using false transient technique, so as to achieve reasonable distribution of flow variables. Subsequently, computations are carried out using global under-relaxation factor $\alpha = 0.1$ to obtain complete convergence.

The accuracy of the solution is concerned with two aspects. Thus, although the flow is truly periodic over $H/2$ distance (90° rotation of the tape) along the axial direction, computations are carried out over $2H$ distance to ensure that the shorter distance periodicity in fact reproduced. Evidence of this will be shown in Section 4. The second aspect concerns grid independence of the solutions. To test this, computations are carried out using 15 (ξ_1) × 10 (ξ_2) × 13 (ξ_3, with $2H$ periodicity) grid at highest Reynolds number (≈ 1100) and Prandtl number ($Pr = 500$) under laminar flow conditions. The grids are then refined to $23 \times 18 \times 25$, $39 \times 32 \times 49$ and $67 \times 62 \times 89$. Since, the values of f, Nu and Re for the last two grids differed by less than 0.5%, all computations are performed with $39 \times 32 \times 49$ grids for $2H$ periodicity and $39 \times 32 \times 13$ grids for the $H/2$ periodicity. Same grid size is used for turbulent flow calculations, however, care has been taken to place the first grid line next to the solid wall at $y^+ \approx 20$.

4. Results and discussion

4.1. Evaluation of Re, f and Nu

The dimensional analysis of the transport equations and the boundary conditions shows that the pitch-averaged friction factor, f, and the Nusselt number, Nu, must bear the following functional relationships: [1]

$$f = f(Re, Y, \delta/a) \tag{21}$$

$$Nu = Nu(Re, Y, \delta/a, Pr) \tag{22}$$

In the present computations, flow variables are solved for a prescribed value of β_p. From the converged solutions, $\bar{u}_3$ is calculated at each cross-section from

$$\bar{u}_3 = \frac{1}{A_c} \int_{A_c} u_3 \, dA_c \tag{23}$$

where A_c is the cross-sectional area. At convergence, $\bar{u}_3$ at different axial stations are observed to be constant up to fourth places of decimal. From $\bar{u}_3$, Re and f are evaluated as

$$Re = \rho \bar{u}_3 a / \mu \tag{24}$$

$$f = \beta_p a / 2\rho \bar{u}_3^2 \tag{25}$$

In the solution of the energy equation, since $H2$ boundary condition is used, the average wall ($\overline{T}_w$) and the bulk temperature (T_b) at every cross-section are calculated as

$$\overline{T}_w = \frac{1}{S_c} \int_{S_c} T_w \, dS \tag{26}$$

$$T_b = \frac{\int_{A_c} u_3 T \, dA_c}{\int_{A_c} u_3 \, dA_c} \tag{27}$$

Since, the heat flux is also axially constant, T_b is observed to increase linearly with x_3 according to the overall energy balance condition. Now, the local (i.e., cross-section averaged) heat transfer coefficient and the Nusselt number are evaluated as

$$h_{x_3} = \frac{q_w}{\overline{T}_w - T_b} \tag{28}$$

$$Nu_{x_3} = h_{x_3} a / k \tag{29}$$

Finally, the pitch-averaged quantities are evaluated as

$$\bar{h} = \frac{1}{H/2} \int_0^{H/2} h_{x_3} \, dx_3 \tag{30}$$

$$Nu = \bar{h} a / k \tag{31}$$

4.2. Experimental data

In order to verify the computed data to be presented in the next section, pressure drop measurements are carried out in an acrylic passage of square cross-section, 9.5 mm sides and 3000 mm long. The first 1000 mm of the duct is provided for the development of the flow and fully developed flow is expected to prevail over the last 2000 mm of the length. The passage is made by milling to form a 9.5 mm deep and 9.5 mm wide groove in a 25 mm thick acrylic sheet. The groove is then covered with 5 mm thick acrylic strip and bolted. The detailed design and fabrication of the duct is available in Ref. [3].

The pressure taps are fixed on the top plate of the duct. These taps consist of a 1.5 mm diameter and 2.5 mm deep hole, followed by a 5 mm diameter and 2.5 mm deep hole. In the later holes, around 50 mm long copper tubes of same outer diameter are press fitted. To make these joints leak proof and permanent, synthetic adhesives are used. Flexible plastic tubes are connected at the end of these copper tubes. Whenever reading from a particular pressure tap is required, the flexible tubes are attached to the manometer. In the set-up, altogether 20 pressure taps are provided to measure the axial variation in pressure. Out of these, 10 pressure taps, at a distance of 100 mm, are located in the developing section (within first 1000 mm), where the pressure drop is expected to be higher. The rest of these taps are mounted in the developed section (the last 2000 mm) at a distance of 200 mm. The pressure drops are measured using manometers with benzyle alcohol, carbon-tetra-chloride, and mercury as working fluids to cover different ranges of Reynolds number. The fully developed friction factors are calculated on the basis of the pressure drop data, measured over the last 2000 mm of length. Thus, even for $Y = 10.28$, nearly 10 pitch lengths could be accommodated in the developing section and hence, the results presented in this paper are indeed for fully developed flow.

Water is used as the working fluid in the present study. The water temperature is measured to calculate the fluid properties. For lower Reynolds number ($100 < Re < 3000$), the fluid is allowed to flow from an overhead tank, where a constant head is maintained.

---

[1] Computations are carried out using $\delta/a = 0$.

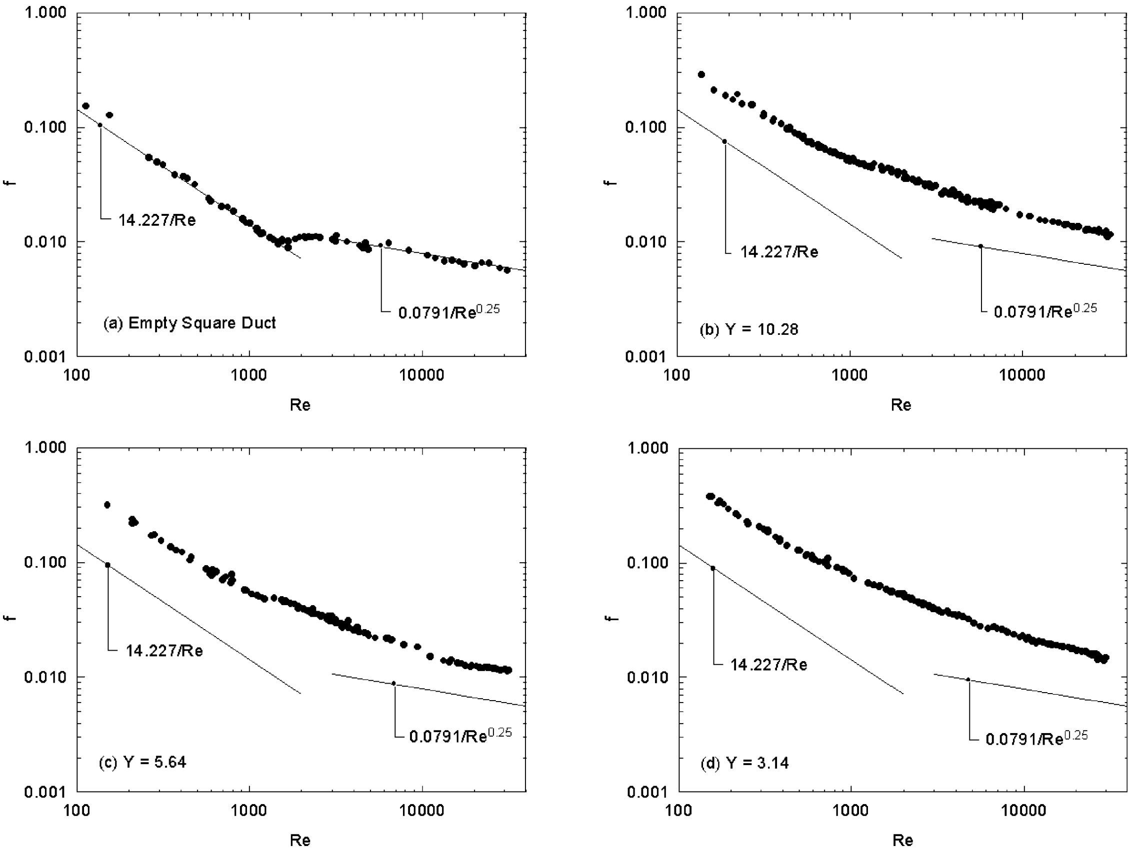

Fig. 3. Experimental friction factor data: (a) empty square duct, (b) $Y = 10.28$, (c) $Y = 5.64$ and (d) $Y = 3.14$.

For higher flow rates, however, the direct discharge from the centrifugal pump is allowed to flow through the test section. The flow rate is calculated by collecting the water in a volumetrically calibrated tank for a period of about 5–10 min, depending upon the flow rate. The uncertainties associated with the present experiment are discussed in detail by Ray [3], which show that, for laminar flow, the maximum uncertainties in Reynolds number and friction factor are within ±4% and ±8% respectively, whereas, for turbulent flow, they are within ±3% and ±6% respectively.

Since the pressure drops are measured at discrete locations and the flow is *periodically* fully developed, it is not possible to exactly estimate the development lengths at different values of Y. However, over the last 2000 mm length, the pressure variation indeed appears to be linear when nearly *corresponding* locations are considered [3]. For lower values of Y, linearity in pressure variation is detected over a much larger length [3]. The measured friction factors for empty square duct and for $Y = 10.28$, 5.64 and 3.14 are shown in Fig. 3. In the experiments tapes are made of 0.3 mm metallic strips, such that, $\delta/a = 0.3/9.5 \approx 0.032$. The data for empty duct show excellent agreement with analytical solutions for laminar flow and with the well established empirical correlations for turbulent flow. The transition Reynolds number range appears to be from 1500 to 3000.

The data for different twist ratios however do not appear to demonstrate any change corresponding to laminar-to-turbulent transition. This trend is typical of twisted tape flows as is reported by Manglik and Bergles [12,13], in a recent review of data on flow in a circular tube with twisted tape insert. The present data however match with the expectation that, at a fixed Reynolds number, as Y decreases (or, twist becomes tighter) the friction factor increases.

4.3. Results for laminar flow

4.3.1. Friction factor

The straight tape represents the limiting case of twisted tape flow, with $Y \rightarrow \infty$. If the tape is inserted such that its two ends along the width touch the opposite sides of the square duct, we obtain flow in a rectangular passage, with aspect ratio 2, under consideration. For this case, secondary flow is absent and the analytical solution [14] is $fRe = 34.983$. The present code yielded fRe within 0.5% of the above value irrespective of the value of β_p (or, Reynolds number). Computations for twisted tape are carried out for Reynolds number up to 1100 since the transition to turbulent flow can be expected at a lower Reynolds number than observed for empty square duct.

Fig. 4 shows the predicted variation of f with Re for different values of twist ratio, Y. The smaller the value of Y, tighter is the twist and thus at a fixed Re, the friction factor increases with reduction of Y. At very low Reynolds numbers, the magnitude of secondary flow (i.e., u_1 and u_2 components) decreases and the friction factor asymptotically approach $Y \to \infty$ line, irrespective of the value of Y. The above data can be correlated with a maximum deviation of ±5% by the following correlation:

$$fRe = 36[1 + 0.15S_{w_s}]^{1/1.3} \tag{32}$$

where S_{w_s} is a notional indicator of the strength of the secondary flow and is given by

$$S_{w_s} = \left(\frac{Re}{Y}\right)^{3/4}\left[\frac{1 + 0.01Y^4}{Y^6}\right]^{1/4} \tag{33}$$

Fig. 5 shows the comparison of the experimental data in the laminar range ($Re \leqslant 1100$). The correlation predicts the experimental data within ±10%. This somewhat greater deviation may be attributed to the effect of tape thickness, which is ignored in the computations and to the probable but negligible non-uniformity of the pitch of the tape in the experiment, which may be considered as an inevitable manufacturing defect. Shah and London [14], for example, estimated the effect of tape thickness in a circular tube to be up to 10%.

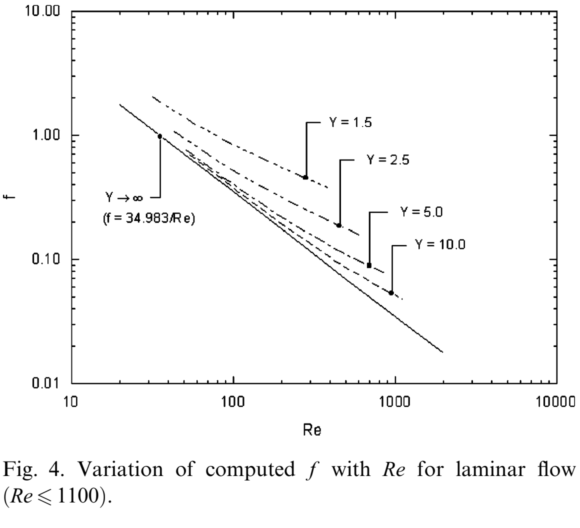

Fig. 4. Variation of computed f with Re for laminar flow ($Re \leqslant 1100$).

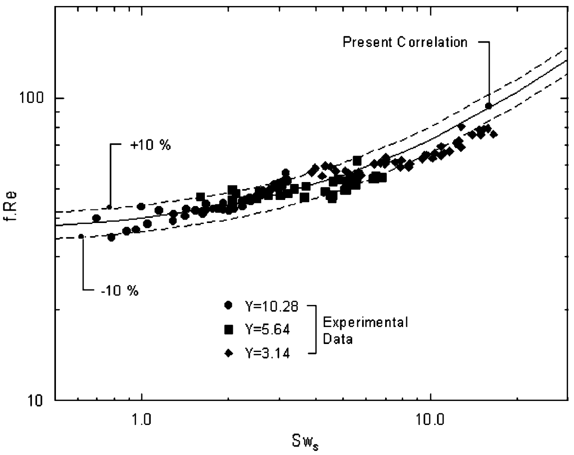

Fig. 5. Comparison of experimental data with present correlation for laminar flow.

4.3.2. Nusselt number

For limiting case of $Y \to \infty$, we have a rectangular duct of aspect ratio 2, with two shorter and one of the longer sides being heated and the other longer side being insulated, since, the tape is assumed to be non-conducting. This case of fully developed laminar flow heat transfer is governed by Poisson's equation for temperature. The equation has been solved analytically by variational method [3], which results in $Nu = 3.96$. The present computer code yielded Nu within 0.2% of the analytical value.

Fig. 6 shows values of local Nusselt number, Nu_{x_3}, for $Pr = 5$ at different Reynolds number and twist ratios, over the length $2H$ (i.e., over four times the distance required for short distance periodicity). The data verify that Nu_{x_3} is indeed periodic with the ratio of maximum to minimum varying between 1.02 and 1.17. Higher the Reynolds number, higher is the ratio. Similar increase in the ratio is also observed with increase in Prandtl number from 1 to 500, when Re is fixed [3]. The most important observation however is that the local Nusselt number peaks at cross-sections where the tape is aligned with the diagonal of the duct (or, when $\theta = 45°$), irrespective of the value of Re, Pr and Y. At these locations the free flow area (see Fig. 1) is maximum and the resistance to cross-flow is minimum. As a result, the fluid that flows around the tape in a narrow region, near the corners of the cross-section, thus provides substantial *wash* in these regions of weakest heat transfer at all other angles. Hence, the local Nusselt number also peaks at these axial locations. This will be more evident from the isotherms, presented in Fig. 8, which clearly indicate the existence of high heat transfer in the *wash* region.

Fig. 7 shows the variation of pitch-averaged Nusselt number, Nu with Re for different Pr and Y. The figure shows that compared to $Nu_\infty = 3.96$, twisted tapes en-

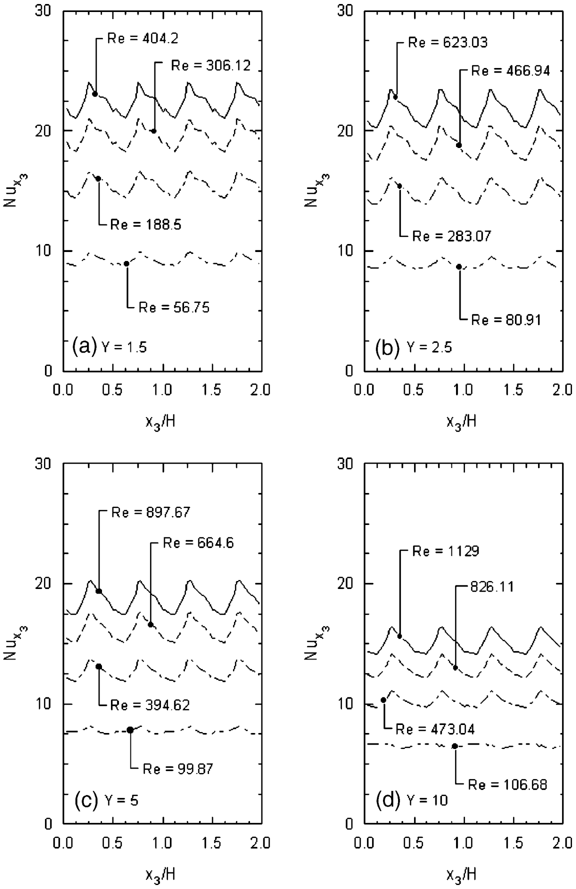

Fig. 6. Variation of Nu_{x_3} with x_3/H for laminar flow $Pr = 5$.

hance heat transfer considerably at high Prandtl numbers. The computed data are correlated within ±10% by the following relation:

$$Nu = 3.96\left[1 + 0.016Pr^{1.05}\left(\frac{Re}{Y}\right)^{1.25}\right]^{1/2.6} \tag{34}$$

4.3.3. Flow structure

Fig. 8 shows typical distribution of secondary flow, axial velocity and temperature at a tight twist ratio $Y = 1.5$, and $Re = 404$, with $Pr = 1$, 50 and 500 for $\theta = 45°$ (i.e., $x_3 = H/4$). In the figure, velocities are normalised with respective to the average axial velocity and the isotherms are plotted for $(T - T_b)/(\overline{T}_w - T_b)$. The figure shows that twisted tape generates high secondary flow (peak value varies from 10% to 110% of the mean axial velocity, depending on the value of Y) and skewed axial velocity profile with peak values located away from the geometric center. The temperature profiles show a large uniform temperature core with greater part of the temperature variation occurring near the duct walls, particularly at higher Prandtl numbers.

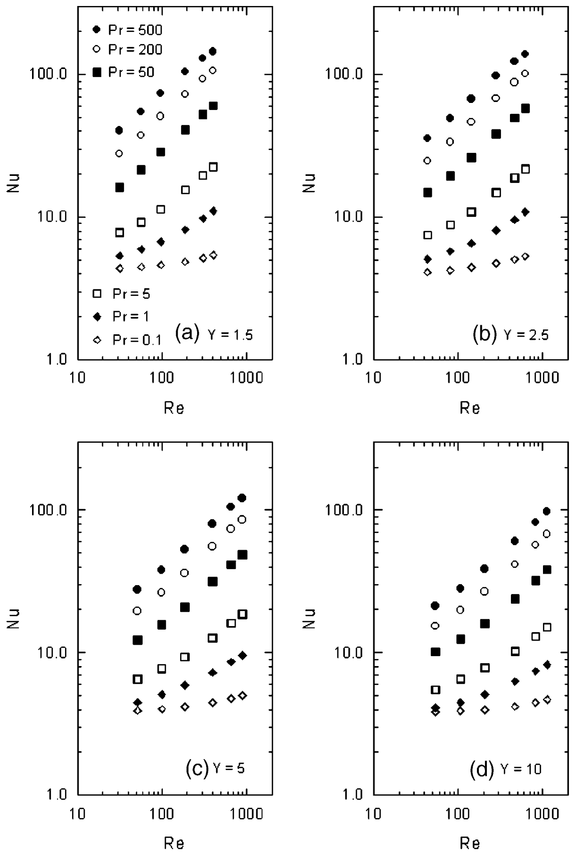

Fig. 7. Raw computation data of Nu for laminar flow.

4.4. Results for turbulent flow

4.4.1. Friction factor

The turbulent flow predictions are carried out with high Reynolds number form of k–ε model of turbulence, with linear eddy viscosity model. Computations are performed for the case of $Y \rightarrow \infty$ (rectangular duct of aspect ratio 2) for $8000 \leqslant Re \leqslant 67000$. The values of predicted f are found to be consistently lower by 12–13%, as compared to the correlated values from $f = 0.0791Re^{-0.25}$ (both f and Re defined on the basis of hydraulic diameter). This is to be expected since the linear eddy viscosity model cannot predict normal stress driven secondary flows encountered in fully developed turbulent flows in ducts with sharp corners [15]. In spite of this inadequacy, the k–ε model is used for the prediction of twisted tape flow, because now the magnitude of the secondary flow is comparable to that of the axial flow and the isotropic turbulence model can still be

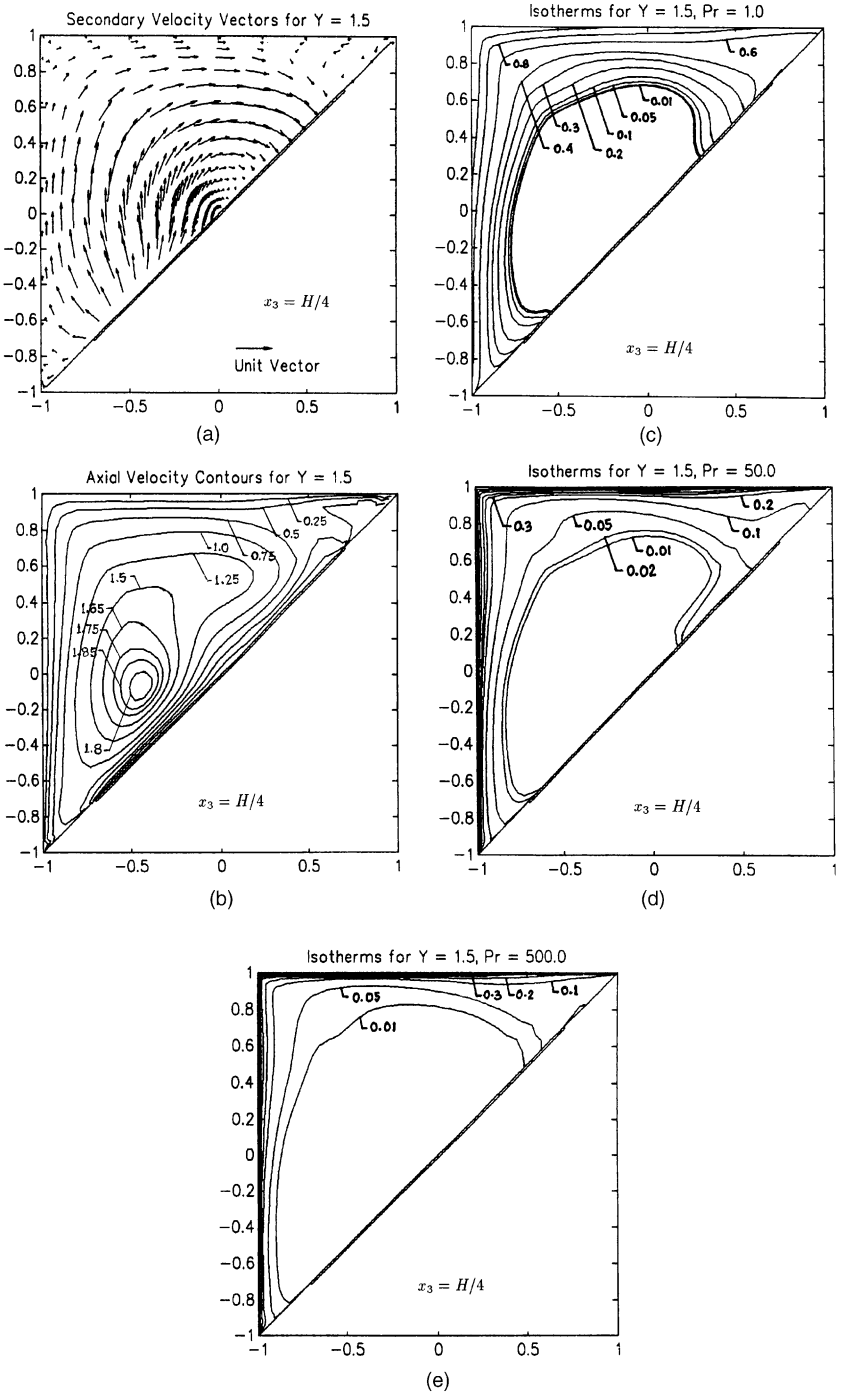

Fig. 8. Distribution of (a) secondary velocity, (b) axial velocity, (c) isotherms for $Pr = 1$, (d) isotherms for $Pr = 50$ and (e) isotherms for $Pr = 500$, for laminar flow with $Y = 1.5$ and $Re = 404$ at $\theta = 45°$.

expected to provide reasonably good prediction of at least the integral quantities, such as, the friction factor and the Nusselt number. The effect of twist ratio is studied by carrying out computations for $Y = 10$, 5, 3.5 and 2.5. The variation of f with Re is presented in Fig. 9. The computed data could be correlated as

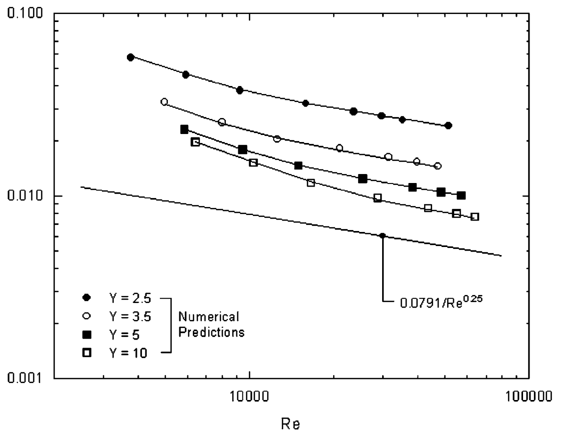

Fig. 9. Variation of computed f with Re for turbulent flow.

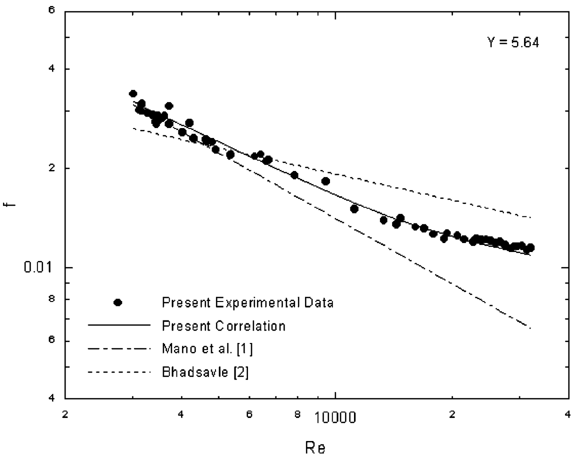

Fig. 11. Comparison of different turbulent flow correlations ($Y = 5.64$).

$$f = \frac{0.0791}{Re^{0.25}}\left[5.5445 - 9.6649\left(\frac{Y}{Y-1}\right) + 5.4428\left(\frac{Y}{Y-1}\right)^2\right]\left[1+\frac{0.0281Y^{0.0393}}{(Re/10^4)^{4.08}}\right]^{0.0732} \quad (35)$$

Fig. 10 shows the comparison of the above correlation with the present experimental data. These data agree within ±15% with the correlation. The present correlation, along with the experimental data, for $Y = 5.64$ is also compared with the correlations proposed by Mano et al. [1] and Bhadsavle [2] in Fig. 11. The figure clearly shows that both the previous correlations compare reasonably well with the experimental data only in narrow ranges of Reynolds number. For example, the correlation of Mano et al. [1] agrees well with the experimental data for $3000 \leqslant Re \leqslant 5500$, whereas, Bhadsavle's [2] correlation provides good agreement for $4000 \leqslant Re \leqslant 7000$. However, for higher Reynolds number, Mano et al. [1] under-predicts and Bhadsavle [2] over-predicts the present experimental data. It is also evident from the figure that the present correlation, obtained from the numerical study, works by far the best for the entire range of Reynolds number ($3000 \leqslant Re \leqslant 32\,000$).

4.4.2. Nusselt number

The Nusselt number data are computed for $Pr = 1$, 5, 20 and 50. To the best of our knowledge, there are no experimental data for rectangular duct (case of $Y \rightarrow \infty$, with one of the longer walls being insulated) available in the open literature. However, comparison with $Nu = 0.023Re^{0.8}Pr^{0.4}$ (Nu and Re both defined on the basis of

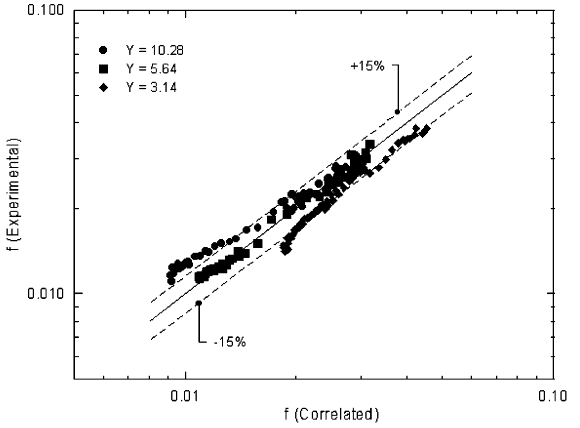

Fig. 10. Comparison of experimental data with present correlation for turbulent flow.

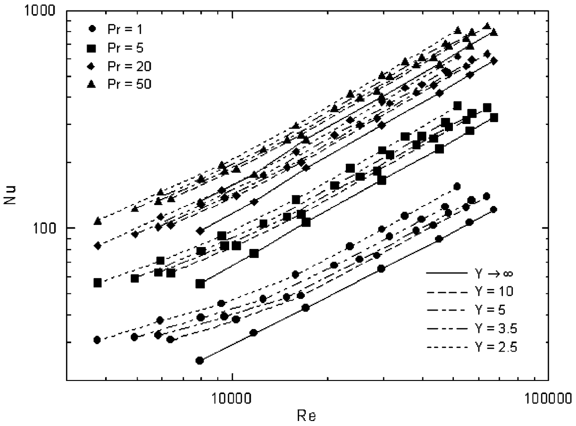

Fig. 12. Variation of computed Nu with Re for turbulent flow.

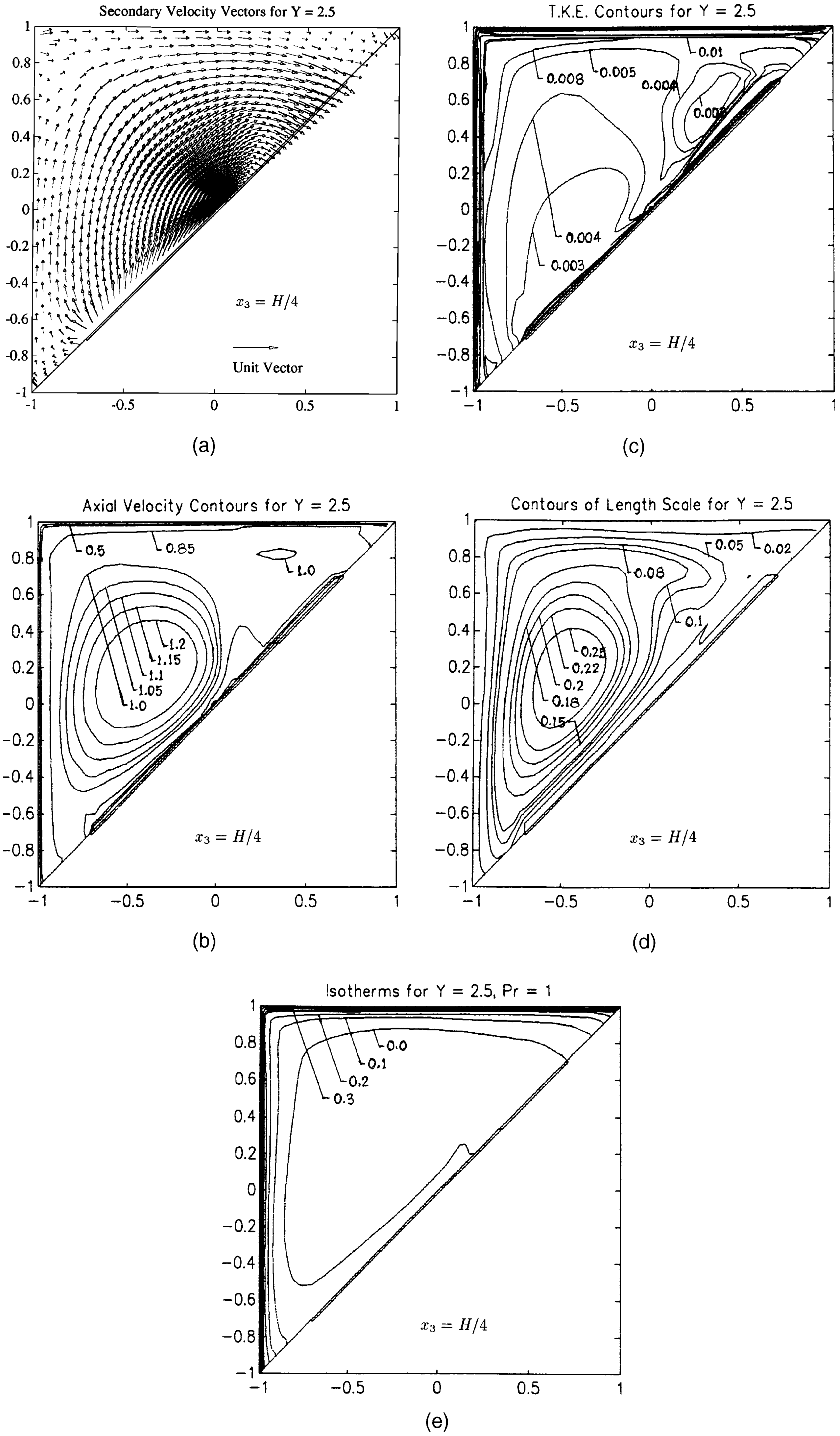

Fig. 13. Distribution of (a) secondary velocity, (b) axial velocity, (c) turbulent kinetic energy, (d) length scale and (e) isotherms for $Pr = 1$, for turbulent flow with $Y = 2.5$ and $Re = 29742$ at $\theta = 45°$.

hydraulic diameter) showed under-prediction by about 15% at $Pr = 1$, but agreement within ±5% at higher Prandtl number.

The computed data for finite twist ratios are presented in Fig. 12. These data could be correlated within −5% and +10% by the following correlation:

$$Nu = cRe^{n_1}\left[1 + \frac{\psi}{Y^{n_2}}\right] \tag{36}$$

where

$$c = 0.023Pr^{0.4}\left[0.5426 + \frac{0.3724}{\sqrt{Pr}} + \frac{0.4628}{Pr}\right] \tag{37}$$

$$n_1 = 0.8546 + \frac{0.043}{\sqrt{Pr}} + \frac{0.0655}{Pr} \tag{38}$$

$$\psi = 0.8654Pr^{-0.18} \tag{39}$$

$$n_2 = 0.8306 - 0.022Pr + 0.0004Pr^2 \tag{40}$$

Since, the variation in the local (i.e., cross-section averaged) Nusselt number is not significant along the length of the duct, it is not presented here.

4.4.3. Flow structure

Typical secondary flow, axial velocity, turbulent kinetic energy, length scale and the temperature distribution for $Y = 2.5$ at $x_3 = H/4$ (i.e., $\theta = 45°$) are presented in Fig. 13. The figure clearly shows the presence of strong secondary circulation in the duct. As expected, the maximum change in the axial velocities occurs near the solid surfaces. As a result, a large portion in the flow domain experiences almost uniform flow, with the maximum axial velocity being of the order of 120% of its mean. The kinetic energy levels are high near the solid surfaces as would be expected. The length scales increase with the distance from the wall and their distribution is dominated by the convection due to secondary flows. The isotherms for $Pr = 1$ show that the maximum temperature variation occurs near the heated walls of the duct and the temperature of the bulk fluid remains almost uniform through out the cross-section.

5. Conclusion

The following are conclusions of the present paper:

1. Periodically fully developed flow and heat transfer in a square duct with twisted tape insert are computed using numerically generated non-orthogonal, non-staggered grids. The novel feature of the numerical method is the use of *smoothing* pressure correction to eliminate the problem of check-board prediction of pressure.
2. The laminar flow friction factor data for $40 \leqslant Re \leqslant 1100$ and $1.5 \leqslant Y \leqslant 10$ are correlated by

   $$f\,Re = 36[1 + 0.15S_{w_s}]^{1/1.3}$$

   where the definition of S_{w_s} is given by Eq. (33). Agreement with the experimental data is within ±10%.
3. The pitch-averaged laminar flow Nusselt number for $Re \leqslant 1100$, $1.5 \leqslant Y \leqslant 10$ and $0.1 \leqslant Pr \leqslant 500$ with non-conducting tape are correlated by

   $$Nu = 3.96\left[1 + 0.016Pr^{1.05}\left(\frac{Re}{Y}\right)^{1.25}\right]^{1/2.6}$$

4. The laminar local Nusselt number shows axial variation occur over $H/2$ length in a repetitive manner, with the ratio of maximum to minimum Nusselt number varying between 1.02 and 1.17. Higher values of the ratio are encountered at higher Re and Pr. The maximum local Nusselt number occurs at a cross-section where the tape is aligned with the diagonal of the duct. In turbulent flow, the axial variation of Nu is not significant.
5. The turbulent flow friction factor data for $4000 \leqslant Re \leqslant 60\,000$ and $2.5 \leqslant Y \leqslant 10$ are correlated by

   $$f = \frac{0.0791}{Re^{0.25}}\left[5.5445 - 9.6649\left(\frac{Y}{Y-1}\right) + 5.4428\left(\frac{Y}{Y-1}\right)^2\right]\left[1 + \frac{0.0281Y^{0.0393}}{(Re/10^4)^{4.08}}\right]^{0.0732}$$

   The agreement with the experimental data is within ±15%.
6. The pitch-averaged Nusselt number for turbulent flow for $4000 \leqslant Re \leqslant 60\,000$, $2.5 \leqslant Y \leqslant 10$ and $1 \leqslant Pr \leqslant 50$ are correlated by

   $$Nu = cRe^{n_1}\left[1 + \frac{\psi}{Y^{n_2}}\right]$$

   where the expressions for c, n_1, ψ and n_2 are given by Eqs. (37)–(40).

Acknowledgements

One of us, Dr. Subhashis Ray would like to thank the authorities of Jadavpur University for granting leave to carry out this research work.

References

[1] Y. Mano, N. Funahashi, S. Kobayashi, M. Kobayashi, Y. Mori, K. Ohhori, I. Nikai, M. Akane, A. Fuji, T. Kaneta, S. Urabe, Development of high temperature plate-fin heat exchanger for phosphoric acid fuel cell power system, in: High Temperature Heat, Exchangers, Hemisphere Publishing Corporation, 1986, pp. 421–432.

[2] V.S. Bhadsavle, Pressure drop characteristics of laminar and turbulent flow through a square duct fitted with full length twisted tapes, B.Tech Project Report, Indian Institute of Technology, Bombay, 1994.

[3] S. Ray, Pressure drop and heat transfer characteristics of flow through square duct with twisted tape insert, Ph.D. Thesis, Indian Institute of Technology, Bombay, 1999.

[4] B.E. Launder, D.B. Spalding, Mathematical Models of Turbulence, Academic Press, London, 1972.

[5] B.E. Launder, D.B. Spalding, The numerical computation of turbulent flows, Comput. Meth. Appl. Mech. Eng. 3 (1974) 269–289.

[6] R.L. Sorenson, A computer program to generate a two-dimensional grid about an airfoil and other shapes by the use of Poisson's equation, NASA Technical Memorandum, NASA TM-81198, 1980.

[7] S.V. Patankar, D.B. Spalding, A calculation procedure for heat mass, and momentum transfer in three-dimensional parabolic flows, Int. J. Heat Mass Transfer 15 (1972) 1787–1806.

[8] S.V. Patankar, Numerical Heat Transfer and Fluid Flow, Hemisphere, Washington, DC, 1980.

[9] A.W. Date, Solution of Navier–Stokes equations on non-staggered grid, Int. J. Heat Mass Transfer 36 (1993) 1913–1922.

[10] A.W. Date, Complete pressure correction algorithm for solution of incompressible Navier-Stokes equations on non-staggered grid, Numer. Heat Transfer, Part B 29 (1996) 441–458.

[11] S. Ray, A.W. Date, A calculation procedure for solution of incompressible Navier-Stokes equations on curvilinear non-staggered grids, Numer. Heat Transfer, Part B 38 (2000) 93–131.

[12] R.M. Manglik, A.E. Bergles, Heat transfer and pressure drop correlations for twisted-tape inserts in isothermal tubes: Part I—laminar flows, ASME J. Heat Transfer 115 (1993) 881–889.

[13] R.M. Manglik, A.E. Bergles, Heat transfer and pressure drop correlations for twisted-tape inserts in isothermal tubes: Part II—transition and turbulent flows, ASME J. Heat Transfer 115 (1993) 890–896.

[14] R.K. Shah, A.L. London, Laminar Flow Forced Convection in Ducts, Advances in Heat Transfer, Suppl. 1, Academic Press, New York, 1978.

[15] B.L. Launder, M. Yang, Prediction of flow and heat transfer in ducts of square cross-section, Inst. Mech. Engrs. Proc. 187 (1973) 455–461.